Nano-Structures & Nano-Objects 35 (2023) 101016

Contents lists available at ScienceDirect

Nano-Structures & Nano-Objects

journal homepage: www.elsevier.com/locate/nanoso

Structure and physicochemical properties of MgB_2 nanosheets obtained via sonochemical liquid phase exfoliation

Santanu Kumar Padhi [a], Xiaolin Liu [b], Maria Carmen Valsania [c], Luca Andreo [c], Angelo Agostino [c], Andrea Alessio [a], Linda Pastero [d], Alessia Giordana [c], Zhilin Wu [b], Giancarlo Cravotto [b], Marco Truccato [a,*]

[a] NIS Interdepartmental Centre and Physics Dept., University of Torino, Via P. Giuria 1, 10125 Torino, Italy
[b] Drugs Dept., University of Torino, Via P. Giuria 9, 10125 Torino, Italy
[c] NIS Interdepartmental Centre and Chemistry Dept., University of Torino, Via P. Giuria 7, 10125 Torino, Italy
[d] NIS Interdepartmental Centre and Earth Science Dept., University of Torino, Via Valperga Caluso 35, 10125 Torino, Italy

ARTICLE INFO

Article history:
Received 25 October 2022
Received in revised form 3 May 2023
Accepted 7 July 2023

Keywords:
Liquid phase exfoliation
MgB_2
Nanosheets
Ultrasound
Optical properties
Hydrogen bonding

ABSTRACT

We have performed ultrasonic liquid phase exfoliation (LPE) of MgB_2 in ethanol and investigated the resulting nano-assemblies as a function of the ultrasound processing time. TEM morphological and structural analysis, along with STM topographic characterization, showed that for short sonication times the exfoliated grains preserve the MgB_2 crystal structure, have a 2D character and produce Moiré patterns corresponding to stacked layers with rotational misalignment. On the other hand, the longest process times result in spheroidal nanoparticles with diameters of the order of 10 nm, which can also coalesce into larger agglomerates. Optical absorbance spectra confirmed that the exfoliated material preserves a metallic nature with a predominant 2D character corresponding to the *ab*-plane, whereas Raman spectra showed the presence of extra-modes induced by 3D symmetry breaking in the exfoliated products, along with indications of some B-H stretching modes. The detection of a positive zeta potential confirms that an active surface hydrogenation process has taken place during sonication. The mechanochemistry of the exfoliation mechanism has been attributed to particle–particle collisions and particle-shockwave interactions originating from the implosive bubble-collapse. The present study provides important information useful for implementing the LPE process in different contexts for MgB_2, like few-layer superconductivity, antibacterial coating and nano-drug preparation.

1. Introduction

Liquid phase exfoliation (LPE) is a simple and versatile processing method to produce atomically thin, scalable quantities of two-dimensional (2D) sheets by direct exfoliation [1–7]. Its primary microscopic mechanism is represented by cavitation bubble collapse, which generates a combination of high energy microjets, interparticle collisions and direct shockwave-solid interactions to yield exfoliated 2D-nanosheets [8–13]. Typically, bulk solids of layered materials are the candidates of choice to undergo the LPE process, but recently also non-layered materials with non-isotropic 3D bonding arrangements (like, for instance, strong in-plane ionic or covalent bonds versus weaker out-of-plane van der Waals or metallic bonding forces) have been successfully treated [14–16].

Generally speaking, 2D-nanostructures have already been obtained from several metal-boride materials and their possible applicability to various fields, like e.g. sensing, electronics, catalysis, energy harvesting, ion transport, hydrogen generation and storage, has been recently discussed [17]. In the specific case of MgB_2, its crystal structure is analogous to that of intercalated graphite, having alternate graphene-like boron basal honeycomb layers (borophene) sandwiched by a close-packed Mg-triangular layer [18,19]. This implies that non-isotropic atomic bonds exist, with strong covalent bonding within each layer and weaker metallic bonding between different layers [20]. For this reason, MgB_2 is expected to preferably cleave at the site of the Mg-B bonds between adjacent layers [21]. In principle, this material could be of interest as a starting point for the production of borophene single layers and indeed several methods have already been used in this direction to obtain MgB_2 nanosheets, including chemical exfoliation by means of chelating agents [22,23], sonication in water [21] or high energy ball milling in an inert atmosphere [24]. However, these methods have shown a deep influence on the MgB_2 structure and properties, resulting in amorphization or high distortion of its crystal structure [21,23], in the heavy reconstruction of the B surfaces [24] and in the

* Corresponding author.
E-mail address: marco.truccato@unito.it (M. Truccato).

https://doi.org/10.1016/j.nanoso.2023.101016

presence of hydroxyl- and oxy-functional groups on the surfaces of these nanosheets [21,22].

On the other hand, the possibility of having nearly-ideal, few-layer MgB_2 nanosheets would be important to discriminate between theoretical models which predict a semiconducting behaviour [25] or a superconducting one (sometimes with a remarkable superconductivity enhancement), providing a good prototype system to understand the real role of surface states in determining superconductivity [26–29]. In this respect, the use of LPE with a solvent to induce minimal perturbation to MgB_2, unlike water, could represent a viable method to achieve this goal. Of course, the efficiency of LPE also depends on other process details and requires a suitable choice of matched surface tension components [30,31], but anhydrous ethanol is a good candidate to minimize chemical interactions and has already been shown to disperse MgB_2 2D-nanosheets in a very effective way [15].

Actually, it should be considered that MgB_2 2D-nanosheets are also being tested in several fields beyond superconductivity, and their use in biomedical applications is at its initial stages of investigation and evaluation. Preliminary indications show that they could be effective and economical for bone tissue engineering [32] and the treatment of some cancers, hypomagnesemia and bacteria-infected wounds [33–36]. Specifically to this biomedical field, the LPE method has great potential as the starting point for further chemical functionalization of the generated MgB_2 2D-nanosheets, also by making use of non-inert solvents. Thereby, it could enable a controlled modification of the properties of nanosheets during LPE to increase biocompatibility, targeted drug delivery or antimicrobial activities [37–40].

However, in the present paper we focus on the LPE method used for MgB_2 in ethanol. The goal consists of understanding the mechanochemistry of the process as a function of its duration and in investigating the features of the MgB_2 nanoparticles and their surface physicochemical attributes in comparison with bulk MgB_2. This represents an important step towards the production of nearly ideal MgB_2 nanosheets, with possible developments both for basic superconductivity studies and for subsequent surface functionalization with a variety of bioadaptive chemical groups to be grafted in a controlled way for desired applications.

2. Materials and methods

MgB_2 powder has been produced by means of the Mg-Reactive Liquid Infiltration (Mg-RLI) method using an amorphous B powder (Sigma Aldrich, Taufkirchen, Germany, nominal purity > 95%, particle size $\leq$ 1 μm) and Mg granules (Alfa Aesar, Kandel, Germany, nominal purity 99.8%, 1.70 mm) as precursors, with a stoichiometric ratio Mg:B = 1.4:2 [37].

These precursors were placed inside a degassed stainless steel container one after the other, in an alternate configuration. Then, the ends of the precursor-filled container were sealed by hydraulic pressing. Before filling with precursors, the steel reaction chamber was degassed at 200 °C for 7 h in a 0.2 L/min Ar flux and then stored in a glove box. Both the precursor and steel container handling were carried out inside the glove box to minimize contamination by oxygen.

The thermal cycle for the material synthesis consisted of heating the sealed container in a quartz furnace up to 800 °C for 6 h. The heating ramp was performed at a rate of 5 °C/min and an intermediate plateau at 150 °C (1 h dwell) was maintained before reaching the final temperature. During the synthesis, a constant Ar flux of 0.2 L/min was maintained.

The sample extraction from the steel container was performed by cutting it to obtain lumpy grains of the product. They underwent XRD measurements and the corresponding Rietveld analysis showed the sample consisted of 98 wt% MgB_2 and 2 wt% MgO (sample code: MBNB06, see Fig.S1 in the Supplementary Information). This grainy mass was manually ground with a mortar and pestle for almost 10 min to obtain a MgB_2 fine powder ready for sonochemical exfoliation activity.

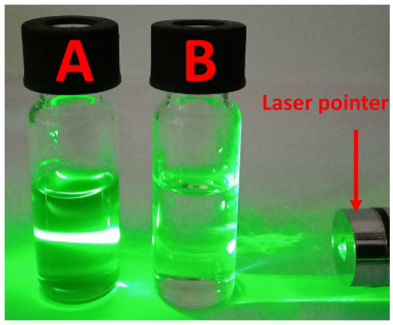

Fig. 1. Observation of light scattering for a green laser beam by (A) the 1 h sonicated product and (B) pure ethanol solvent. The Tyndall scattering is visible for the sonicated dispersion only.

The LPE was carried out by means of a cup horn cavitating tube (Danacamerini srl, Turin, Italy) working at 19.5 kHz and 75 W (input power). The cavitating tube was cooled with refrigerated fluid.

Three different batches of 200 mg MgB_2 powder were mixed in 20 mL ethanol (anhydrous, assay ≥99%, Sigma Aldrich) and sonicated for 1, 2 and 3 h duration, respectively. Ice water circulation around the titanium alloy transducers plus a 10 min off-cycle every 30 min of continuous sonication were employed to dissipate solvent heat generated by the ultrasonic treatment. The exfoliated mass was separated by centrifugation (Allegra 64 R centrifuge, Beckman Coulter) at 15000 rpm for 1 min.

Confirmation of the presence of nanoparticles in the supernatant liquid dispersion after only 1 h of sonication can be observed in Fig. 1; the Tyndall effect can be clearly observed along the path of the laser light in the sonicated dispersion only, implying successful exfoliation.

In order to study the nanoparticle features, the exfoliated ethanol dispersions were deposited by drop casting over lacey-carbon films on copper TEM grids. Their microstructural and aggregation features were investigated with a JEOL 3010 UHR TEM microscope (JEOL Ltd., Tokyo, Japan), operated at an acceleration voltage of 200 kV. The subsequent image analysis was performed with TEM digital micrograph software. On the other hand, the general structure of grains of the MgB_2 precursor powder was studied by means of a table-top compact Scanning Electron Microscope COXEM EM-30 for secondary electron images.

Nanoparticle STM data were acquired with a Danish Micro-Engineering (Herlev, Denmark) SPM Microscope (DME Igloo) equipped with a DS95-50E scanner (scan volume 50 × 50 × 5 μm) and Pt-Ir tips. Exfoliated supernatant samples were prepared by drop-casting 0.1 mL of the MgB_2 suspension in ethanol onto sapphire substrates coated with 20 nm Au and drying them under an incandescent lamp. Topographic imaging was performed at a constant tunnelling current of 2 nA with 0.1 V bias and under Ar flux to remove humidity. Scanning areas were selected at the rim of the dried droplets to increase statistics.

Optical absorption data were acquired with a Perkin Elmer Lambda 900 spectrophotometer. Samples were collected in quartz cuvettes of 0.1 cm optical path. Raman spectroscopic investigations of the exfoliated products were performed using a Bruker Vertex 70 spectrometer, equipped with the RAMII accessory and a Ge detector, by exciting the samples with a Nd:YAG laser source

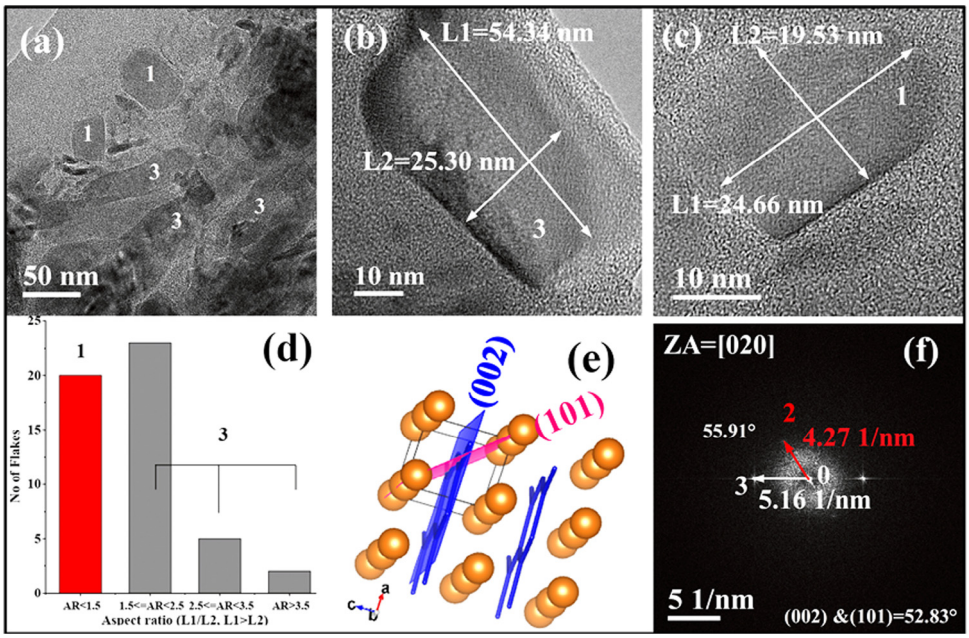

Fig. 2. TEM observations of the MgB_2 exfoliated layers obtained after 1 h sonication. (a) Bright Field (BF) general view of the exfoliated layers on the TEM grid: the labels "1" indicate particles with similar sizes along both directions, the labels "3" indicate particles more elongated in one direction. (b) Zoom-in of an individual particle of type "3". (c) Zoom-in of an individual particle of type "1". (d) Histogram of the statistical distribution of the particle aspect ratio (AR) calculated over more than 50 particles: the red bar refers to type "1" particles, whereas the grey bars are associated with type "3" particles. (e) Sketch of the MgB_2 crystal structure, with B atoms represented by the blue network and Mg atoms by the orange spheres: the (002) and (101) crystal planes are also highlighted. (f) Fast Fourier Transform (FFT) of panel (c): the main components of the reciprocal lattice have been identified as the vector $\overrightarrow{02}$ (red arrow, modulus equal to 4.27 nm^{-1}) and the vector $\overrightarrow{03}$ (white arrow, modulus equal to 5.16 nm^{-1}). The angle measured between these two vectors is equal to about 55.9°. (For interpretation of the references to colour in this figure legend, the reader is referred to the web version of this article.)

(1064 nm) and with a minimum resolution of 4 cm^{-1}. Zeta potential investigations were carried out employing a Zetasizer Nano Z instrument (Malvern Panalytical). The exfoliated dispersion was taken in a disposable folded capillary cell for measurement, whereas its pH value was recorded with an 827 pH meter by Metrohm, Italy.

3. Results and discussion

The TEM observations concerning the 1 h sonicated MgB_2 supernatant dispersion are summarized in Fig. 2.

The general view displayed in Fig. 2(a) shows that particles with different morphologies are present. Indeed, two types of almost isotropic particles can be detected, i.e. with a different aspect ratio (AR) of the particle sizes along the different directions (L1 and L2): AR = L1/L2 ≤ 1.5 (which have been labelled as type "1" particles) and more elongated particles with AR > 1.5 (which have been labelled as type "3" particles). Their typical sizes range between approximately 20 and 100 nm (see Fig. 2(a)) and the statistical distribution of their aspect ratio shows that about 40% of the particles falls in the isotropic type "1" category, whereas the remaining 60% belongs to the elongated type "3". Closer inspections of typical type "3" and typical type "1" particles can be carried out in Fig. 2(b) and (c), respectively.

The Fast Fourier Transform of Fig. 2(c) is reported in Fig. 2(f) for further analysis. It can be noticed that, on top of the amorphous halo around the origin, two main crystalline contributions can be detected. The most apparent one is represented by the vector $\overrightarrow{03}$ (white arrow in Fig. 2(f)), whose modulus is equal to 5.16 nm^{-1}, corresponding to a d-spacing value for the crystal planes d = 1.94 Å. According to the MgB_2 standard diffraction card ICDD PDF-2#65-3383, the expected d-spacing for the (002) planes is $d_{(002)}$ = 1.767 Å. The difference between the measured and expected values is about 9.7%, which falls within the typical uncertainty for d-spacing measurements via TEM. Moreover, another weaker crystalline contribution can be observed in Fig. 2(f) as the red vector $\overrightarrow{02}$, whose modulus is equal to 4.27 nm^{-1}. This implies a corresponding d-spacing for the crystal planes d = 2.34 Å. According to the same standard diffraction card for MgB_2, the expected d-spacing for the (101) planes is $d_{(101)}$ = 2.128 Å. Again, the difference between the expected and the measured values is about 10%, which is acceptable. Finally, the angle measured via TEM between these two vectors is about 55.9°, which compares favourably with the theoretically expected value of about 53° for the angle between the (002) and the (101) planes. Fig. 2(e) displays a scheme of the crystal structure of MgB_2, highlighting the orientation of the (002) and (101) crystalline planes, which allows visualization of the angle between them and making a direct comparison with the orientation of the vectors $\overrightarrow{03}$ and $\overrightarrow{02}$ of Fig. 2(f), respectively.

Therefore, the match between the d-spacing values and the angle allows the conclusion that the nanoparticle observed in Fig. 2(c) is really a nanoparticle consisting of MgB_2. Moreover, the detection of the (002) and (101) planes implies that, in principle, both of planes can represent termination surfaces of these nanoparticles. However, this gives no special information about the chemical nature of the B- or Mg-termination surfaces of the nanoparticles, leaving both of them equally probable. More insight about the structure of the MgB_2 nanoparticles resulting from 1h-sonication can be obtained from the High-Resolution TEM images shown in Fig. 3.

It is possible to observe that the particle reported in Fig. 3(a) is about 80 nm in size and actually consists of a stack of 6 different layers, which are labelled as L1 to L6. The FFT of the area corresponding to the red box is displayed in Fig. 3(b), where, on top of the amorphous halo, 3 main crystalline components can be detected: the vector $\overrightarrow{01}$ (red arrow, modulus equal to 3.96 nm^{-1}), the vector $\overrightarrow{02}$ (white arrow, modulus equal to 4.45 nm^{-1}) and the

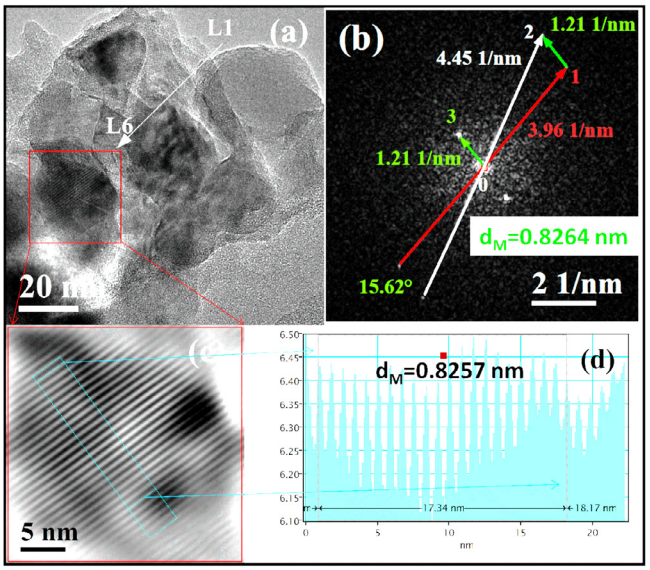

Fig. 3. HRTEM imaging of the MgB_2 exfoliated layers obtained after 1 h sonication. (a) overview of a 2D-nanosheet consisting of 6 stacked layers (L1 to L6); (b) FFT of the portion of panel (a) corresponding to the L6 layer and surrounded by the red box: the main components of the reciprocal lattice have been identified as the vector $\overrightarrow{01}$ (red arrow, modulus equal to 3.96 nm^{-1}), the vector $\overrightarrow{02}$ (white arrow, modulus equal to 4.45 nm^{-1}) and the vector $\overrightarrow{03}$ (green arrow, modulus equal to 1.21 nm^{-1}). The angle measured between $\overrightarrow{01}$ and $\overrightarrow{02}$ is equal to about 15.6°; (c) Inverse FFT of panel (b) after masking the vectors $\overrightarrow{01}$ and $\overrightarrow{02}$; (d) line profile of the fringes visible in panel (c): their period is equal to 0.8257 nm. (For interpretation of the references to colour in this figure legend, the reader is referred to the web version of this article.)

vector $\overrightarrow{03}$ (green arrow, modulus equal to 1.21 nm^{-1}), with an angle between $\overrightarrow{01}$ and $\overrightarrow{02}$ equal to about 15.6°. The corresponding d-spacing for the crystalline planes are 2.53, 2.25 and 8.26 Å, respectively. By comparing these values with the ones reported in the above mentioned ICDD card, it is easy to identify the vector $\overrightarrow{01}$ as the reciprocal vector (100) ($d_{(100)} = 2.671$ Å) and the vector $\overrightarrow{02}$ as the reciprocal vector (101) ($d_{(101)} = 2.128$ Å), since in both cases the expected and measured moduli agree to within a very reasonable uncertainty of about 5%.

However, the interpretation of vector $\overrightarrow{03}$ requires some more discussion. Indeed, in the crystal structure of MgB_2 the longest interplanar distance is $d_{(001)} = 3.522$ Å, which is less than 50% of the measured value. This observation unequivocally implies that this contribution cannot originate from the MgB_2 crystal structure itself. On the other hand, the observation of the presence of up to 6 different layers opens the way to a correct interpretation. Indeed, it is well-known that two lattices superimposed with some misalignment angle can originate interference patterns with a new periodicity, i.e. the so-called Moiré patterns. The general mathematical formula for the period d_M of the Moiré pattern generated by two lattices with periods d_{01} and d_{02}, featuring a misalignment angle α_{102}, is reported in Eq. (1):

$$d_M = \frac{d_{01}d_{02}}{\sqrt{d_{01}^2 + d_{02}^2 - 2d_{01}d_{02}\cos\alpha_{102}}}. \quad (1)$$

Table 1 lists the features of the reciprocal vectors identified in Fig. 2(b) with more precise measurements. Based on these data, Eq. (1) predicts a value for the period d_M of the Moiré pattern generated by the vectors $\overrightarrow{01}$ and $\overrightarrow{02}$ $d_M = 8.066$ Å. This value agrees very well (i.e. within about 2%) with the experimental d-spacing of the vector $\overrightarrow{03}$ reported in Table 1. Therefore, it can be concluded that the MgB_2 nanoparticle of Fig. 3(a) actually consists of a few stacked nanosheets slightly misaligned to each other.

Table 1
Reciprocal vectors and corresponding angles shown in Fig. 3(b).

Reciprocal vector	Modulus (1/nm)	d-spacing (Å)	Angle (°) with respect to vector $\overrightarrow{01}$
$\overrightarrow{01}$	3.967	2.521	0
$\overrightarrow{02}$	4.450	2.247	15.62
$\overrightarrow{03}$	1.211	8.258	76.16

This situation can be visualized in a more clear way by taking the inverse FFT of Fig. 3(b), while masking the vectors $\overrightarrow{01}$ and $\overrightarrow{02}$, which is shown in Fig. 3(c). In this picture the fringes of the Moiré pattern corresponding to the vector $\overrightarrow{03}$ are very apparent and their period reported in Fig. 3(d) is practically the same as the d-spacing of the vector $\overrightarrow{03}$, as expected.

To obtain a clear confirmation about the layered nature of the exfoliated nanoparticles, we have compared TEM and STM acquisitions for the 1 h sonicated supernatant dispersion. The corresponding results are shown in Fig. 4. Even if the nanoparticles considered are obviously not exactly the same in both measurements, it is possible to see that on a typical length scale of about 200 nm, what in the TEM image seems to be a nanosheet really corresponds to a layer about 14 nm in thickness in the STM image, with an average surface roughness $S_{rms} = 1.5$ nm, that has to be compared with the value $S_{rms} = 0.58$ nm of the substrate (see Fig. S2 in Supplementary Information). Therefore, the 2D nature of the nanosheets observed in the TEM image is confirmed, with a typical length-to-height ratio greater than 10.

Fig. 5(a) and (d) display a TEM overview of the exfoliated MgB_2 nanosheets obtained after 2 h of sonication. The extension of some individual nanosheets, identified as domains with coherent lattice fringes, is indicated by the violet arrows: It is possible to notice that practically all of the sheets look like isotropic flakes with characteristic sizes below 10 nm. This seems to indicate that longer sonication times induce higher fragmentation of the MgB_2 nanosheets.

The FFTs of the regions surrounded by red boxes and labelled as "2" in Fig. 5(a) and (d) are displayed in Fig. 5(b) and (e), respectively. Even over such small regions, it is possible to identify many crystalline contributions corresponding to many reciprocal vectors. However, practically all of them lay on two circles, meaning that two moduli are dominant, even if the reciprocal vector orientations can be very different. This situation is typical of a polycrystalline sample. In Fig. 5(b) and (e) two representative vectors have been highlighted. The vector $\overrightarrow{01}$ has a modulus of 3.67 and 3.80 nm^{-1} in Fig. 5(b) and (e), respectively, corresponding to d-spacing values of 2.72 and 2.63 Å, respectively. Again, these vectors can be identified with the reciprocal vector (100) of the ICDD card, which predicts a theoretical value $d_{(100)} = 2.671$ Å that is just 2% different from the measured one. The vector $\overrightarrow{03}$ has a modulus of 4.26 nm^{-1} in both Figs. 5(b) and 5(e), corresponding to a d-spacing value d = 2.35 Å. This vector can be identified with the reciprocal vector (101), whose d-spacing is $d_{(101)} = 2.128$ Å, in reasonable agreement (about 10% difference) with the measured value. Interestingly, the (101) and (100) Bragg reflections are the two most intense ones expected from a polycrystalline MgB_2 sample, which makes the present spot indexing fully self-consistent. The additional features emerging from Fig. 5(b) and (e) are represented by the vectors $\overrightarrow{02}$. Again, they can be interpreted as Moiré patterns originating from superimposed, misaligned MgB_2 nanosheets. Indeed, according to Eq. (1), the periods of the Moiré patterns generated by the vectors

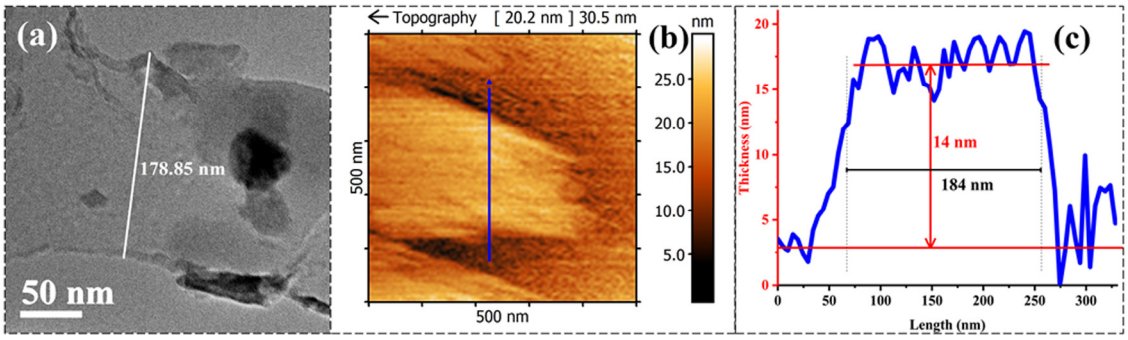

Fig. 4. Comparison between TEM and STM measurements of the 1 h sonicated supernatant dispersion. (a) TEM BF morphology and (b) STM topographic map of similar nanosheets with the same typical length scale of about 200 nm. (c) STM profile of a nanosheet, taken along the blue line shown in panel (b). (For interpretation of the references to colour in this figure legend, the reader is referred to the web version of this article.)

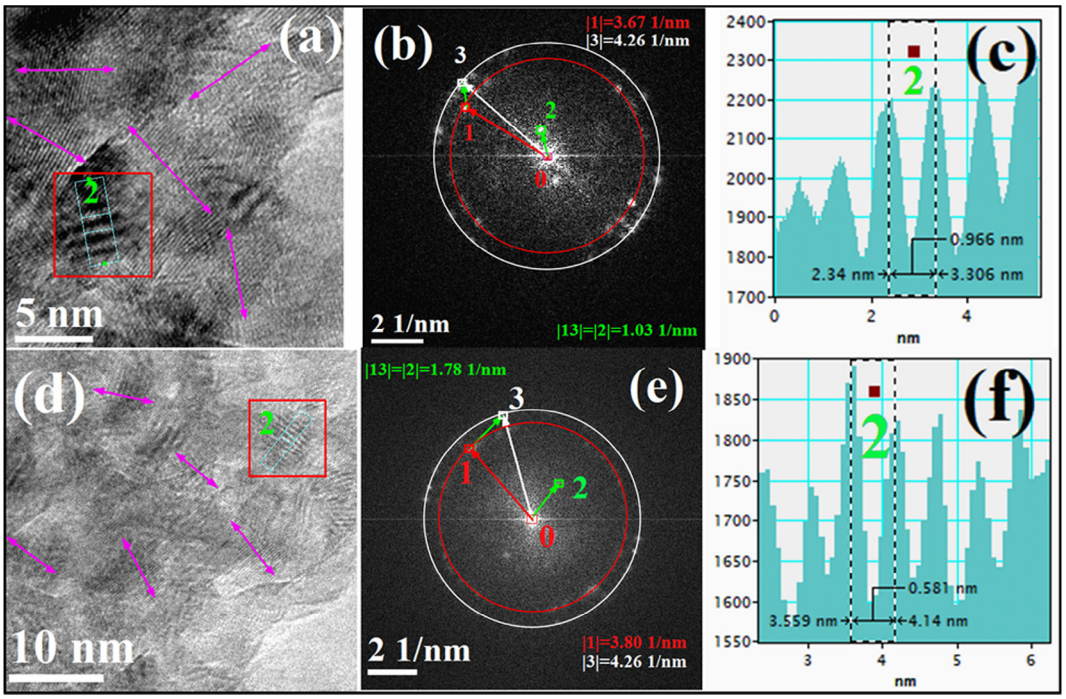

Fig. 5. HRTEM imaging of the MgB_2 exfoliated layers obtained after 2 h sonication, (a) and (d) overview of the nanoparticles at different magnifications: violet lines indicate the approximate extension of some individual sheets; (b) and (e) FFT of the regions surrounded by red boxes and labelled as "2" in panels (a) and (d), respectively. In both panels, vectors $\overrightarrow{01}$ and $\overrightarrow{03}$ represent the contribution from the planes of the MgB_2 crystal structure, whereas vector $\overrightarrow{02}$ represents the Moiré pattern emerging from stacked misaligned MgB_2 nanosheets; (c) and (f) intensity profiles measured along a line normal to the Moiré fringes observed in the regions "2" of panels (a) and (d), respectively. (For interpretation of the references to colour in this figure legend, the reader is referred to the web version of this article.)

$\overrightarrow{01}$ and $\overrightarrow{03}$ are equal to $d_M = 9.620$ Å and $d_M = 5.568$ Å for Fig. 5(b) and (e), respectively. On the other hand, the periods measured in Fig. 5(c) and (f) for the fringes visible in the regions labelled as "2" in Fig. 5(a) and (d) are $d_M = 9.66$ Å and $d_M = 5.81$ Å, in good agreement with the expected values.

In order to compare the TEM observations with the STM ones for the 2 h sonicated supernatant dispersion, we focussed on the length scale of 100 nm. Fig. 6 shows the corresponding observations for two different nanosheets with approximately the same shape and size. The STM topographic map indicates that this nanosheet is about 7 nm in height, with a width-to-height ratio of at least 15 (depending on the profile orientation) and an average surface roughness $S_{rms} = 0.8$ nm. These measurements confirm the 2D nature of the 2 h exfoliated nanosheets, too.

One of the liquid dispersions was sonicated for 3 h and then treated in two different ways. Part of the product was dried from ethanol by keeping it at 80 °C for 48 h in air: the corresponding TEM images are shown in Fig. 7(a) and (b). Another part of the dispersion was tested as usual by taking 5 mL of the supernatant liquid obtained via centrifugation and casting it on the TEM grid: the corresponding images are shown in Fig. 7(c) and (d).

Fig. 7(a) shows that the desiccated dispersion results in a set of aggregated particles with sizes between 5 and 10 nm, which stick on the edge of a non-transparent bulky particle. Considering the size of this bulky particle and the fact that the pristine MgB_2 powder consists of grains with an average size of about 1.4 μm (see Fig. S3 in Supplementary Information), it is natural to identify this bulky particle as a grain of the pristine powder that underwent no or minimal fragmentation process during the 3 h sonication.

Focussing on the edge region of this aggregate (see Fig. 7(b)), it is possible to clearly distinguish the single crystallites and their fringes, with a measurement of the d-spacing equal to $d = 2.706$ Å. This spacing matches well with the one of the (100) planes $d_{(100)} = 2.671$ Å, confirming that this is the dominant orientation for these MgB_2 planes and that the aggregate on the

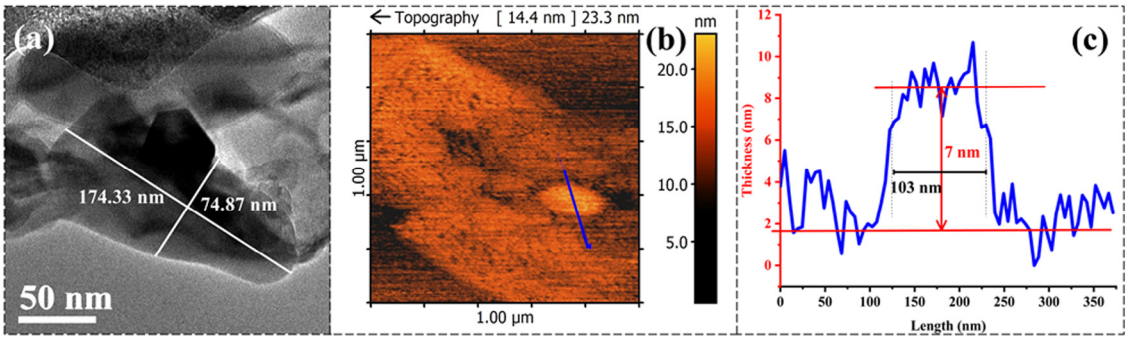

Fig. 6. Comparison between TEM and STM measurements of the 2 h sonicated supernatant dispersion. (a) TEM BF morphology and (b) STM topographic map of similar nanosheets with the same typical length scale of about 100 nm. (c) STM profile of a nanosheet, taken along the blue line shown in panel (b). (For interpretation of the references to colour in this figure legend, the reader is referred to the web version of this article.)

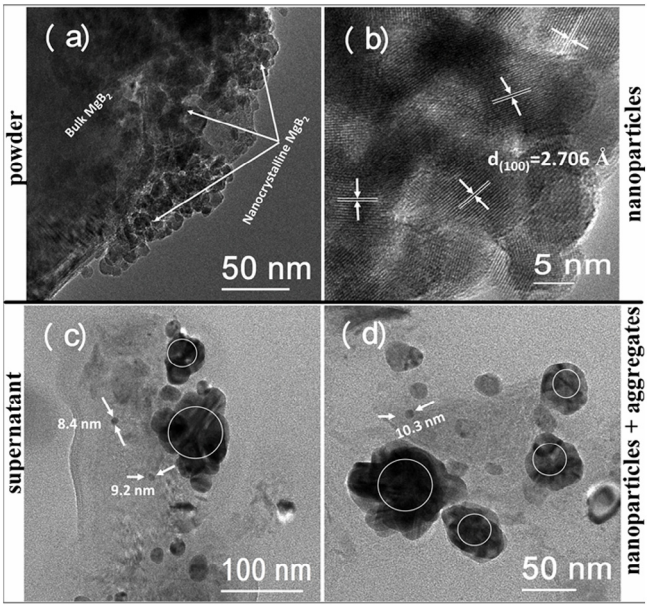

Fig. 7. TEM imaging of the MgB_2 exfoliated particles obtained after 3 h sonication. (a) low-magnification BF image representing both the bulk and the edge regions of the MgB_2 nanoparticle aggregate obtained via oven-drying; (b) HR image of the edge region of panel (a): lattice fringes with d = 2.706 Å are indicated; (c) and (d) low-magnification BF images of MgB_2 nanoparticles obtained from a centrifuge-derived supernatant drop. Some approximately circular particles with diameters of about 10 nm are indicated by white arrows. Bigger particles, about one order of magnitude larger in size and formed by many aggregated particles, are highlighted by white circles.

edge of the bulky particle consists of densely packed MgB_2 single nanocrystals.

Fig. 7(c) and (d) show that these nanoparticles, about 5–10 nm in size, can also be observed in an isolated form in the case of the supernatant solution. As we will discuss in the following, these isolated particles can be indicated as primary particles and their aggregation can lead to the formation of more complex bodies about one order of magnitude larger, as indicated by the white circles in Fig. 7(c) and (d).

To gain further insight about the nature of the isolated nanoparticles observed in the case of the supernatant solution, we carried out a comparison between TEM and STM observations, which is summarized in Fig. 8. In the TEM image, these particles show a rounded shape with a diameter ranging between 10 and 40 nm, approximately (Fig. 8(a)). Nanoparticles with analogous shape and size have also been detected in the STM image and a typical profile is shown in Fig. 8(c). It is clear that in this case it is no longer possible to define a "flat" top surface of the nanoparticle and that the prolonged sonication process has resulted in objects resembling spheroidal or ellipsoidal shapes.

All of these observations lead to the following picture for the present sonication process, which is graphically summarized in Fig. 9 and discussed in the following.

As it is well-known, the LPE technique is based on the cavitation bubble-collapse mechanism. Generally speaking, the microscopic processes that can take place during this kind of treatment are represented by: (i) interparticle collisions, (ii) surface damage (e.g. from micro-jets or particle collisions or direct shockwave damage) and iii) particle fragmentation (mostly from direct shockwave-particle interactions) [13–16,18]. In principle, all of these mechanisms can coexist, but the dominant process largely depends on the suspension particle density and secondly on the length of the sonication. Indeed, for instance, the surface damage by micro-jets rapidly decreases when the mean size of the solid surface becomes less than the resonant bubble dimensions just before collapsing [16].

As a matter of fact, many of previous research efforts employing sonication on MgB_2 have resulted in chemically modified 2D-layered products with different structures, stoichiometries and functionalities [21,23,41]. For instance, the use of a high load of MgB_2 spherical particles (about 45 µm in diameter) in decalin has induced interparticle coalescence by fusion just within 1 h of sonication treatment [42].

On the other hand, very few reports exist about direct bulk-MgB_2 exfoliation [15,43]. Our study, being intended to investigate the ability of sonication to deliver nanostructured MgB_2 products with unmodified stoichiometry and minimal surface contamination, has used a low particle concentration for the suspension (i.e. 1 g/100 mL) and a prolonged sonication time to facilitate particle fragmentation.

During the sonication process, vapour bubbles have nucleated and grown in the low-density regions generated by the ultrasound pressure waves until they have reached the resonant size of about 150-200 µm in diameter (see Fig. 9(a)). At this point, the bubbles have collapsed into a core of a few nm in size, where the local pressure conditions are equivalent to a temperature of the order of $T = 5000$ K (Fig. 9(b)). In these very high-energy-density conditions, many radical species can be produced by fragmentation of the ethanol molecules, but the most abundant one is represented by the H^+ species [44] (see Fig. 9(c)). Of course, these radicals diffuse from the collapsed core into the bulk of the liquid and can also recombine into neutral molecules, nevertheless they are continuously created by subsequent collapses in a dynamical way, resulting in a higher amount of H^+ ions available during sonication.

Concerning the exfoliation mechanism, it should be considered that the average size of the grains of the precursor powder is

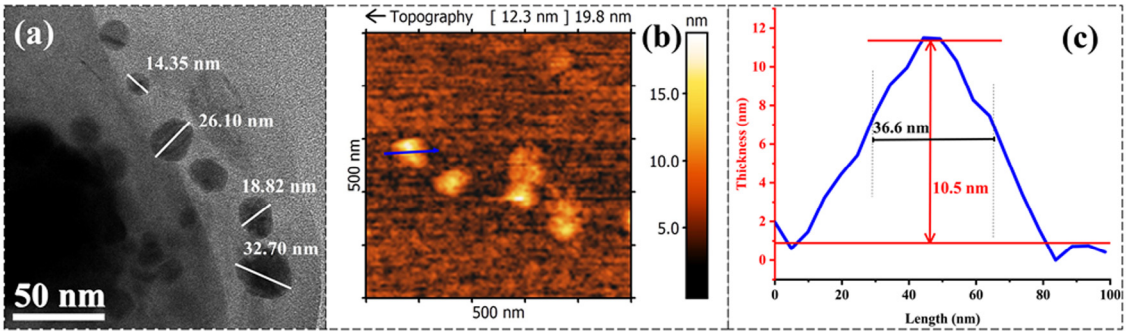

Fig. 8. Comparison between TEM and STM measurements of the 3 h sonicated supernatant dispersion. (a) TEM BF morphology and (b) STM topographic map of similar nanoparticles with the same typical length scale of about 30 nm. (c) STM profile of a nanoparticle, taken along the blue line shown in panel (b). (For interpretation of the references to colour in this figure legend, the reader is referred to the web version of this article.)

just 1.4 μm, to be compared with the size of about 150-200 μm for the resonant bubbles in ethanol just before collapsing. This implies that direct surface damage of the grains by the microjets is expected to be highly inefficient and therefore negligible. On the other hand, MgB_2 grains located close to a collapsed core should be highly affected by the pressure fronts of the generated shockwaves: the discontinuities in the fluid pressure and temperature are expected to result in grain fragmentation and exfoliation, depending on the reciprocal orientation between the grain surface and the wave front (Fig. 9(d)). Another process taking place during sonication is represented by particle–particle collisions. Indeed, even if the microjets originating from bubble collapse are ineffective in directly hitting the MgB_2 grain surfaces, they produce local microstreams that during the collapse can accelerate the grains located close to the bubble walls over the distance of the bubble diameter (i.e. about 150-200 μm) up to a striking speed of approximately 1200 m/s. This can lead to a particle–particle collision between the accelerated particle and another stationary grain located close to the opposite wall of the collapsed bubble. However, since pristine MgB_2 grains are typically 2D-hexagonal in shape, the probability of head-on collisions is expected to be negligible. Other reciprocal orientations corresponding to large glancing-angle collisions should lead to surface damage (and thereby to fragmentation) for one of the particles and to possible exfoliation for the other one (Fig. 9(e)).

Indeed, a comparison between Fig. 2(a) and Fig. 7(a)–(d) indicates a morphological degradation of MgB_2 due to nanosheet fragmentation, likely due to these large glancing-angle particle–particle collisions or to direct shockwave-particle interaction. This observation seems also to exclude a grain growth process derived from individual particle head-on collisions, confirming that this process has really a negligible probability.

Fig. 7(c) and (d) show that this fragmentation process continues up to the point when the cavitation-generated nanoparticles reach a minimum size of approximately 10 nm, which can be indicated as the size of the primary particles. At that point (which in our experiment occurred after about 2 h of sonication) particle coalescence becomes the dominant process: aggregation takes place between primary particles, each of them retaining its crystalline nanostructure (see e.g. Fig. 7(b)), via particle–particle collision, up to the formation of agglomerates with a typical size of 50–100 nm.

Finally, it should also be considered that at any stage of these processes, the H^+ ions resulting from ethanol fragmentation can be adsorbed on the MgB_2 nanoparticle surfaces at convenient atomic sites, producing positively charged nanoparticles (see Fig. 9(f)). Experimental evidences of this fact will be discussed in the following.

In order to gain more knowledge about the physical properties of these MgB_2 nanoparticles, we have investigated their optical response in the dispersion stage. Fig. 10 displays their UV–VIS optical absorption spectra resulting after the correction for the baseline absorbance of the solvent (i.e. ethanol).

From the point of view of the general optical properties of MgB_2 in its normal state, anisotropic plasma edge frequencies $\omega_{p,a}$ and $\omega_{p,c}$ have been reported in the in-plane and out-of-plane crystallographic directions, respectively, along with the presence of a feature related to the $\sigma \rightarrow \pi$ interband transition [45–49]. However, their details strongly depend on sample characteristics, like doping and crystal quality [50,51]. In this respect, we consider that the LPE method used for our sample preparation, even if already starting from high-purity MgB_2 raw materials [37], should have further enriched the purity of the individual MgB_2 nanoparticles because a much smaller exfoliation rate is expected for typical impurities like MgO, whose ionic bonds make it isotropic. For this reason, we prefer to compare our optical results with the ones obtained for high-quality epitaxial MgB_2 films.

Fig. 10 shows that all of the three suspensions share the presence of the same feature located at about 489 nm, which is fixed at $\omega_{p,a} = 20449\ cm^{-1}$ and represents a small "shoulder" (hence the label "s" in Fig. 10) of another broader peak, which has been labelled as "P". In terms of energy, the "shoulder" corresponds to $E = 2.54$ eV and has been associated to the plasma frequency of the quasi-2D in-plane σ-bands within the framework of a simple Drude model for the optical conductivity [52]. Apparently, this plasma edge undergoes no shift as a function of the sonication duration, which means on the one hand that the relevant parameters of the charge carriers (like their density) are unaffected, and on the other hand that the average size of the MgB_2 nanoparticles in all of the samples is too large to observe quantum size effects [53,54].

Concerning the broad peak "P", its centre is positioned at about $22925\ cm^{-1}$, corresponding to about $E = 2.84$ eV. In high-quality epitaxial films, the region in the range 2.55–2.90 eV has been associated with the ab-plane $\sigma \rightarrow \pi$ interband transition, with a centre at approximately 2.78 eV [49,55]. This fact induces the origin of peak "P" to be ascribed to the $\sigma \rightarrow \pi$ transition. It is also interesting that the position of this peak seems to be insensitive to the duration of the sonication process, whereas its height increases on increasing the sonication time and finally it becomes dominant with respect to the shoulder "s". Since the presence of quantum size effects has already been excluded, a reasonable interpretation could be represented by the hypothesis that the accumulation of defects in the MgB_2 nanosheets on increasing the sonication time also increases the interband scattering rate, inducing an increase of the optical absorbance. Therefore, these optical data, on the whole, confirm that the MgB_2 nanoparticles obtained via LPE preserve a *metallic* (albeit defective) nature with a predominant 2D character corresponding to the ab-plane,

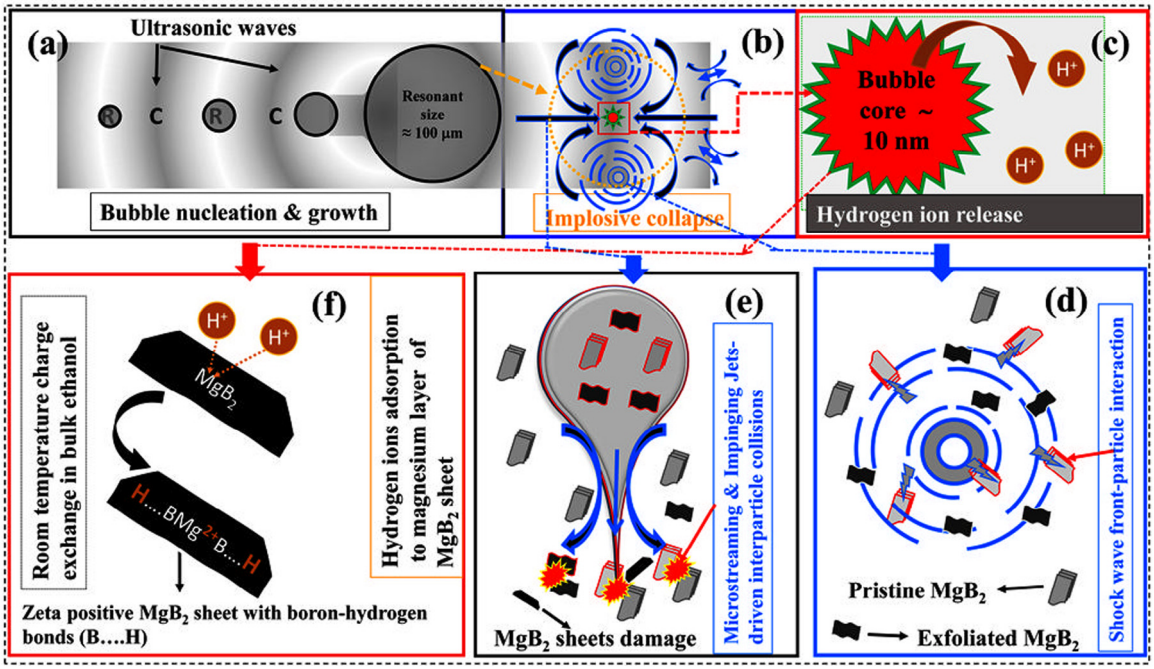

Fig. 9. Schematic overview of the exfoliation physicochemical process taking place in our experiments. (a) Micro-bubble nucleation and growth in the rarefied regions of the liquid; (b) implosive bubble collapse into a nanometric core after reaching the resonant size of 150-200 μm; (c) high-energy-density conditions achieved in the collapsed core (equivalent to $T \approx 5000$ K) produce solvent radical species, the most abundant being H^+; (d) shockwave fronts generated by the collapsed core interact with the particles nearby, resulting in exfoliation or fragmentation (depending on reciprocal orientation); (e) particle–particle collisions induced by microstreams and microjets originating from the bubble implosion: particles are transported and accelerated by the microjets and collide with other stationary particles in the bulk solvent; (f) diffusion of H^+ ions out of the collapsed core and subsequent adsorption on the surface of exfoliated sheets.

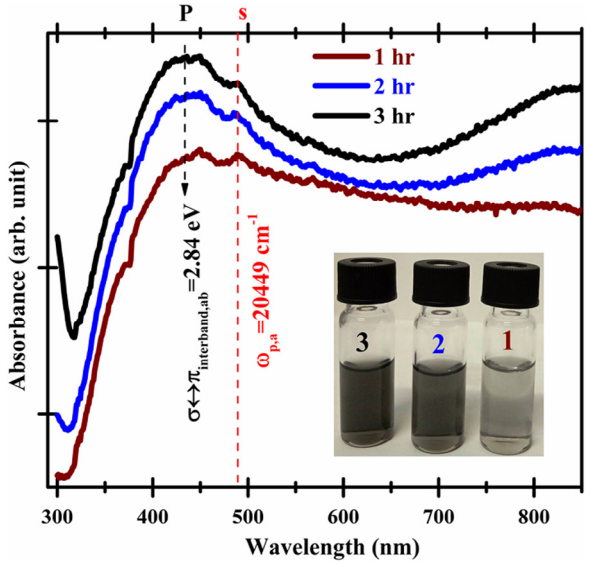

Fig. 10. UV–Visible optical absorption spectra of the supernatant liquids obtained after 1 h (wine curve), 2 h (blue curve) and 3 h (black curve) of MgB_2 sonication processes. The inset shows the glass vials containing the nano-MgB_2 supernatant liquids collected for these measurements. Vertical dashed lines represent a guide to the eye to highlight important physical features. (For interpretation of the references to colour in this figure legend, the reader is referred to the web version of this article.)

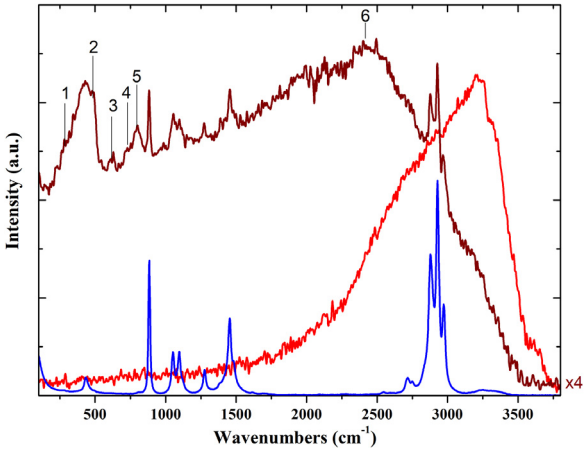

Fig. 11. Raman spectra of the 3 h sonicated MgB_2 dispersion in ethanol (wine curve) and of the corresponding precursor bulk-MgB_2 powder (red curve). Spectral features important for lattice vibrations and surface coordination are numbered from 1 to 6. The blue curve represents the spectral data collected for pure ethanol. (For interpretation of the references to colour in this figure legend, the reader is referred to the web version of this article.)

but without reaching a size range where quantum confinement effects become detectable.

Fig. 11 reports the Raman spectroscopy data measured for the precursor MgB_2 powder and for the 3 h sonicated MgB_2 dispersion in ethanol, in order to elucidate some physicochemical features of the MgB_2 nanoparticles revealed by their low-energy lattice excitations.

For MgB_2 bulk samples (space group I6/mmm), the factor-group analysis predicts four modes at the Γ point: B_{1g}, E_{2g}, A_{2u} and E_{2u}, of which only E_{2g} is Raman active. This mode is generally observed as a broad asymmetric peak around 605 cm^{-1} (75 meV) [56–58], but in the case of our measurements (red curve) it cannot be clearly distinguished from the background. Instead, the spectrum of the bulk MgB_2 shows an intense fluorescence signal at high wavenumbers (from about 2000 to 3500 cm^{-1}), which makes it difficult to recognize other signals.

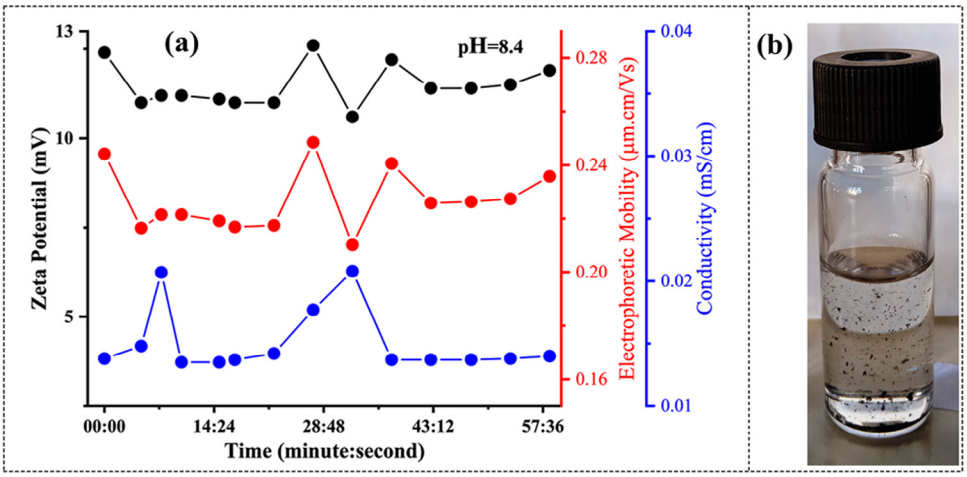

Fig. 12. (a) Physicochemical measurements of 1 h sonicated MgB_2 nanoparticles in ethanol as a function of time: zeta potential (black solid circles), electrophoretic mobility (red solid circles) and electrical conductivity (blue solid circles); (b) photographic snapshot of 1 h sonicated MgB_2 nanoparticle aggregates observed in the laboratory environment after 48 h of storage (photograph taken just after few seconds of manual shaking). (For interpretation of the references to colour in this figure legend, the reader is referred to the web version of this article.)

This problem could be related to the small size of the hexagonal-like platelets of this bulk sample. Indeed, it has been reported that Raman spectra of bulk MgB_2 can be very sensitive to acquisition and sample conditions, and that larger grain sizes typically enhance the observation of well-defined Raman peaks [56,58].

On the other hand, in the spectrum of the 3 h sonicated MgB_2 dispersion (wine curve), more signals are observed. Apart from the peaks corresponding to ethanol, the most important contributions to the spectrum are observed at 300, 500, 610, 730 and 800 cm^{-1} (labelled as peaks n.1, n.2, n.3, n.4 and n.5, respectively). On the basis of the literature, the feature at 610 cm^{-1} can be identified with the well-known E_{2g} stretching mode involving the in-plane displacement of B atoms, which is strongly coupled with the σ electronic band [56–58]. Concerning the other peaks, it is important to mention that, on the basis of experimental IR and Raman data, and also DFT calculations, it has been proposed that a reduced symmetry in the lattice can induce the presence of extra peaks [56]. Actually, the measured positions of the extra peaks correspond approximately to the ones reported for the PDOS calculated in MgB_2 super-lattices with reduced symmetry and so they can be correlated with the presence of few-layer sheets with a distorted lattice, as also testified by the TEM and STM analyses.

It is also worth noting that this spectrum shows fluorescence, albeit different from that of the bulk sample. In this case the position of the maximum of fluorescence emission (around 2436 cm^{-1}, i.e. peak n.6) corresponds to the range of intense B-H stretching modes [59,60]. Therefore, this is an indication that a surface hydrogenation process could take place during sonication, as expected from the H^+ production and adsorption mechanisms shown in Fig. 9(c) and (f). To confirm this hypothesis, we performed a measurement of the zeta potential over a timeframe of 1 h for the 1 h sonicated supernatant solution. The corresponding results are reported in Fig. 12.

It is possible to notice that no time dependence can be observed for the measured quantities over the selected timescale, implying that all of the data are statistically homogeneous and provide the average values of 11.4 ± 0.6 mV, 0.23 ±0.01 μm cm/Vs and 15 ± 2 μS/cm for the zeta potential, the electrophoretic mobility and the electrical conductivity, respectively. Concerning the zeta potential, it should be noticed that its positive sign confirms the Raman indications about the presence of adsorbed H^+ ions on the surface of the nanoparticles, different from what is typically observed in exfoliation experiments in water, where the zeta potential is negative [21]. On the contrary, our experimental situation seems to be more similar to the one of nanodiamonds, where the presence of graphite-like planes with sp^2 bonds at their surfaces promotes nanoparticle hydrogenation [61]. However, the relatively small average value of the zeta potential of our colloidal dispersions corresponds to an incipient instability. Indeed, Fig. 12(b) clearly shows how flocculation starts within 48 h from sonication.

4. Conclusions

We have successfully demonstrated a sonication process to induce exfoliation of high-purity MgB_2 powders into nanoparticles. The evolution of the products from few-layer MgB_2 nanosheets to 3D agglomerates of nanograins with increasing the sonication time has been monitored, with indications that particle-shockwave and particle–particle interactions represent the dominant mechanisms during the exfoliation and aggregation stages, respectively. TEM, STM and spectroscopic investigations have revealed that the obtained MgB_2 nanoparticles preserve their crystal structure and their metallic nature with an enhancement of their 2D features, most likely induced by their few-layer thickness. No chemical alteration has been detected in MgB_2 because of the low-frequency sonication process, apart from hydrogen-termination of the nanoparticle surfaces. The corresponding colloidal dispersions show incipient instability and start flocculating within 48 h.

This study provides important preliminary information useful to implement the LPE process in different applications of MgB_2, like basic superconductivity studies, antibacterial coating or nano-drug preparation.

CRediT authorship contribution statement

Santanu Kumar Padhi: Conceptualization, Methodology, Investigation, Formal analysis, Visualization, Writing – original draft. **Xiaolin Liu:** Validation, Resources. **Maria Carmen Valsania:** Investigation, Formal analysis. **Luca Andreo:** Investigation, Formal analysis. **Angelo Agostino:** Validation, Resources. **Andrea Alessio:** Investigation, Software. **Linda Pastero:** Investigation, Formal analysis. **Alessia Giordana:** Investigation, Formal analysis. **Zhilin Wu:** Investigation, Formal analysis. **Giancarlo Cravotto:** Resources, Supervision. **Marco Truccato:** Resources, Writing – review & editing, Supervision, Project administration, Funding acquisition.

Declaration of competing interest

The authors declare that they have no known competing financial interests or personal relationships that could have appeared to influence the work reported in this paper.

Data availability

Data will be made available on request.

Acknowledgements

S.K.P., A. Agostino, A. Alessio and M.T. acknowledge the Italian Ministry of Education, University and Research (MIUR) and the EU for financial support, project ERA.NET II—BIOMB. S.K.P., A. Alessio and M.T. also acknowledge partial support from the "Departments of Excellence" (L. 232/2016) grant, funded by MIUR, Italy. S.K.P. is also thankful to Prof. Roberto Rabezzana for help in the observation of Tyndall scattering. Prof. Francesco Turci is also duly acknowledged for instrument training and for the Z-potential measurement obtained with the equipment acquired by the Interdepartmental Center "G. Scansetti" for Studies on Asbestos and Other Toxic Particulates with a grant from Compagnia di San Paolo, Torino, Italy.

Appendix A. Supplementary data

Supplementary material related to this article can be found online at https://doi.org/10.1016/j.nanoso.2023.101016.

References

[1] J.N. Coleman, M. Lotya, A. O'Neill, S.D. Bergin, P.J. King, U. Khan, K. Young, A. Gaucher, S. De, R.J. Smith, I.V. Shvets, S.K. Arora, G. Stanton, H.-Y. Kim, K. Lee, G.T. Kim, G.S. Duesberg, T. Hallam, J.J. Boland, J.J. Wang, J.F. Donegan, J.C. Grunlan, G. Moriarty, A. Shmeliov, R.J. Nicholls, J.M. Perkins, E.M. Grieveson, K. Theuwissen, D.W. McComb, P.D. Nellist, V. Nicolosi, Two-dimensional nanosheets produced by liquid exfoliation of layered materials, Science 331 (2011) 568–571, http://dx.doi.org/10.1126/science.1194975.

[2] V. Nicolosi, M. Chhowalla, M.G. Kanatzidis, M.S. Strano, J.N. Coleman, Liquid exfoliation of layered materials, Science 340 (2013) 1226419, http://dx.doi.org/10.1126/science.1226419.

[3] L. Niu, J.N. Coleman, H. Zhang, H. Shin, M. Chhowalla, Z. Zheng, Production of two-dimensional nanomaterials via liquid-based direct exfoliation, Small 12 (2016) 272–293, http://dx.doi.org/10.1002/smll.201502207.

[4] F.I. Alzakia, S.C. Tan, Liquid-exfoliated 2D materials for optoelectronic applications, Adv. Sci. 8 (2021) 2003864, http://dx.doi.org/10.1002/advs.202003864.

[5] V. Paolucci, G. D'Olimpio, L. Lozzi, A.M. Mio, L. Ottaviano, M. Nardone, G. Nicotra, P. Le-Cornec, C. Cantalini, A. Politano, Sustainable liquid-phase exfoliation of layered materials with nontoxic polarclean solvent, ACS Sustain. Chem. Eng. 8 (2020) 18830–18840, http://dx.doi.org/10.1021/acssuschemeng.0c04191.

[6] H. Chacham, J.C.C. Santos, F.G. Pacheco, D.L. Silva, R.M. Martins, J.P. Del'Boccio, E.M. Soares, R. Altoé, C.A. Furtado, F. Plentz, B.R.A. Neves, L.G. Cançado, Controlling the morphology of nanoflakes obtained by liquid-phase exfoliation: Implications for the mass production of 2D materials, ACS Appl. Nano Mater. 3 (2020) 12095–12105, http://dx.doi.org/10.1021/acsanm.0c02598.

[7] C.A. Howard, Exfoliating large monolayers in liquids, Nature Mater. 20 (2021) 130–131, http://dx.doi.org/10.1038/s41563-020-00907-y.

[8] M. Dular, T. Požar, J. Zevnik, R. Petkovšek, High speed observation of damage created by a collapse of a single cavitation bubble, Wear. 418–419 (2019) 13–23, http://dx.doi.org/10.1016/j.wear.2018.11.004.

[9] S. Barcikowski, A. Plech, K.S. Suslick, A. Vogel, Materials synthesis in a bubble, MRS Bull. 44 (2019) 382–391, http://dx.doi.org/10.1557/mrs.2019.107.

[10] T. Prozorov, R. Prozorov, K.S. Suslick, High velocity interparticle collisions driven by ultrasound, J. Am. Chem. Soc. 126 (2004) 13890–13891, http://dx.doi.org/10.1021/ja049493o.

[11] S.J. Doktycz, K.S. Suslick, Interparticle collisions driven by ultrasound, Science 247 (1990) 1067–1069, http://dx.doi.org/10.1126/science.2309118.

[12] R. Pecha, B. Gompf, Microimplosions: Cavitation collapse and shock wave emission on a nanosecond time scale, Phys. Rev. Lett. 84 (2000) 1328–1330, http://dx.doi.org/10.1103/PhysRevLett.84.1328.

[13] M. Dular, B. Stoffel, B. Širok, Development of a cavitation erosion model, Wear 261 (2006) 642–655, http://dx.doi.org/10.1016/j.wear.2006.01.020.

[14] D. Sahoo, B. Kumar, J. Sinha, S. Ghosh, S.S. Roy, B. Kaviraj, Cost effective liquid phase exfoliation of MoS_2 nanosheets and photocatalytic activity for wastewater treatment enforced by visible light, Sci. Rep. 10 (2020) 10759, http://dx.doi.org/10.1038/s41598-020-67683-2.

[15] M.S. Gilliam, A. Yousaf, Y. Guo, D.O. Li, A. Momenah, Q.H. Wang, A.A. Green, Evaluating the exfoliation efficiency of quasi-2D metal diboride nanosheets using hansen solubility parameters, Langmuir 37 (2021) 1194–1205, http://dx.doi.org/10.1021/acs.langmuir.0c03138.

[16] H. Kaur, R. Tian, A. Roy, M. McCrystall, D.V. Horvath, G. Lozano Onrubia, R. Smith, M. Ruether, A. Griffin, C. Backes, V. Nicolosi, J.N. Coleman, Production of quasi-2D platelets of nonlayered iron pyrite (FeS_2) by liquid-phase exfoliation for high performance battery electrodes, ACS Nano. 14 (2020) 13418–13432, http://dx.doi.org/10.1021/acsnano.0c05292.

[17] H. Gunda, L.E. Klebanoff, P.A. Sharma, A.K. Varma, V. Dolia, K. Jasuja, V. Stavila, Progress, challenges, and opportunities in the synthesis, characterization, and application of metal-boride-derived two-dimensional nanostructures, ACS Mater. Lett. 3 (2021) 535–556, http://dx.doi.org/10.1021/acsmaterialslett.1c00086.

[18] M.E. Jones, R.E. Marsh, The preparation and structure of magnesium boride, MgB_2, J. Am. Chem. Soc. 76 (1954) 1434–1436, http://dx.doi.org/10.1021/ja01634a089.

[19] E. Nishibori, M. Takata, M. Sakata, H. Tanaka, T. Muranaka, J. Akimitsu, Bonding nature in MgB_2, J. Phys. Soc. Japan 70 (2001) 2252–2254, http://dx.doi.org/10.1143/JPSJ.70.2252.

[20] M.R. Koblischka, S. Roth, A. Koblischka-Veneva, T. Karwoth, A. Wiederhold, X.L. Zeng, S. Fasoulas, M. Murakami, Relation between crystal structure and transition temperature of superconducting metals and alloys, Metals 10 (2020) 158, http://dx.doi.org/10.3390/met10020158.

[21] S.K. Das, A. Bedar, A. Kannan, K. Jasuja, Aqueous dispersions of few-layer-thick chemically modified magnesium diboride nanosheets by ultrasonication assisted exfoliation, Sci. Rep. 5 (2015) 10522, http://dx.doi.org/10.1038/srep10522.

[22] R. Saraswat, A.L. James, K. Jasuja, High yield synthesis of boron-based nanosheets, Adv. Appl. Ceram. 118 (2019) 209–216, http://dx.doi.org/10.1080/17436753.2019.1584481.

[23] A.L. James, K. Jasuja, Chelation assisted exfoliation of layered borides towards synthesizing boron based nanosheets, RSC Adv. 7 (2017) 1905–1914, http://dx.doi.org/10.1039/C6RA26658D.

[24] S. Li, H. Gunda, K.G. Ray, C.-S. Wong, P. Xiao, R.W. Friddle, Y.-S. Liu, S. Kang, C. Dun, J.D. Sugar, R.D. Kolasinski, L.F. Wan, A.A. Baker, J.R. Lee, J.J. Urban, K. Jasuja, M.D. Allendorf, V. Stavila, B.C. Wood, Spontaneous dynamical disordering of borophenes in MgB_2 and related metal borides, Nat. Commun. 12 (2021) 6268, http://dx.doi.org/10.1038/s41467-021-26512-4.

[25] B.Z. Xu, S.P. Beckman, Quantum confinement induced band gaps in MgB_2 nanosheets, 2D Mater. 3 (2016) 031003, http://dx.doi.org/10.1088/2053-1583/3/3/031003.

[26] B. Ao, Z. Zhang, T. Tang, Y. Zhao, Potential enhancement of superconductivity in MgB_2 nanosheets: First-principles calculations, Chem. Phys. Lett. 591 (2014) 185–188, http://dx.doi.org/10.1016/j.cplett.2013.11.045.

[27] J. Bekaert, A. Aperis, B. Partoens, P.M. Oppeneer, M.V. Milošević, Evolution of multigap superconductivity in the atomically thin limit: Strain-enhanced three-gap superconductivity in monolayer MgB_2, Phys. Rev. B. 96 (2017) 094510, http://dx.doi.org/10.1103/PhysRevB.96.094510.

[28] J. Bekaert, L. Bignardi, A. Aperis, P. van Abswoude, C. Mattevi, S. Gorovikov, L. Petaccia, A. Goldoni, B. Partoens, P.M. Oppeneer, F.M. Peeters, M.V. Milošević, P. Rudolf, C. Cepek, Free surfaces recast superconductivity in few-monolayer MgB_2: Combined first-principles and ARPES demonstration, Sci. Rep. 7 (2017) 14458, http://dx.doi.org/10.1038/s41598-017-13913-z.

[29] Z. Liu, B. Wang, Biaxial strain engineering on the superconducting properties of MgB_2 monolayer, Mater. Chem. Phys. 290 (2022) 126637, http://dx.doi.org/10.1016/j.matchemphys.2022.126637.

[30] J. Shen, Y. He, J. Wu, C. Gao, K. Keyshar, X. Zhang, Y. Yang, M. Ye, R. Vajtai, J. Lou, P.M. Ajayan, Liquid phase exfoliation of two-dimensional materials by directly probing and matching surface tension components, Nano Lett. 15 (2015) 5449–5454, http://dx.doi.org/10.1021/acs.nanolett.5b01842.

[31] J. Shen, J. Wu, M. Wang, P. Dong, J. Xu, X. Li, X. Zhang, J. Yuan, X. Wang, M. Ye, R. Vajtai, J. Lou, P.M. Ajayan, Surface tension components based selection of cosolvents for efficient liquid phase exfoliation of 2D materials, Small 12 (2016) 2741–2749, http://dx.doi.org/10.1002/smll.201503834.

[32] R. Abhinandan, S. Pranav Adithya, D. Saleth Sidharthan, K. Balagangadharan, N. Selvamurugan, Synthesis and characterization of magnesium diboride nanosheets in alginate/polyvinyl alcohol Scaffolds for bone tissue

engineering, Colloids Surf. B Biointerfaces 203 (2021) 111771, http://dx.doi.org/10.1016/j.colsurfb.2021.111771.
[33] M. Fan, Y. Wen, D. Ye, Z. Jin, P. Zhao, D. Chen, X. Lu, Q. He, Acid-responsive H_2-releasing 2D MgB_2 nanosheet for therapeutic synergy and side effect attenuation of gastric cancer chemotherapy, Adv. Healthc. Mater. (2019) http://dx.doi.org/10.1002/adhm.201900157.
[34] Z. Jin, D. Chen, P. Zhao, Y. Wen, M. Fan, G. Zhou, Y. Wang, Q. He, Coordination-induced exfoliation to monolayer bi-anchored MnB2 nanosheets for multimodal imaging-guided photothermal therapy of cancer, Theranostics 10 (2020) 12.
[35] T.A. Ranathunge, D.G.G.P. Karunaratne, R.M.G. Rajapakse, D.L. Watkins, Doxorubicin loaded magnesium oxide nanoflakes as pH dependent carriers for simultaneous treatment of cancer and hypomagnesemia, Nanomaterials 9 (2019) 208, http://dx.doi.org/10.3390/nano9020208.
[36] Y. Meng, L. Chen, Y. Chen, J. Shi, Z. Zhang, Y. Wang, F. Wu, X. Jiang, W. Yang, L. Zhang, C. Wang, X. Meng, Y. Wu, W. Bu, Reactive metal boride nanoparticles trap lipopolysaccharide and peptidoglycan for bacteria-infected wound healing, Nature Commun. 13 (2022) 7353, http://dx.doi.org/10.1038/s41467-022-35050-6.
[37] S.K. Padhi, N. Baglieri, V. Bonino, A. Agostino, L. Operti, N.D. Batalu, M.C. Chifiriuc, M. Popa, M. Burdusel, M.A. Grigoroscuta, G.V. Aldica, D. Radu, P. Badica, M. Truccato, Antimicrobial activity of MgB_2 powders produced via reactive liquid infiltration method, Molecules 26 (2021) 4966, http://dx.doi.org/10.3390/molecules26164966.
[38] P. Badica, N.D. Batalu, M.C. Chifiriuc, M. Burdusel, M.A. Grigoroscuta, G. Aldica, I. Pasuk, A. Kuncser, M. Enculescu, M. Popa, L.G. Marutescu, I. Gheorghe, O. Thamer, C. Bleotu, G. Gradisteanu Pircalabioru, L. Operti, V. Bonino, A. Agostino, M. Truccato, MgB_2 powders and bioevaluation of their interaction with planktonic microbes, Biofilms, and Tumor Cells, J. Mater. Res. Technol. 12 (2021) 2168–2184, http://dx.doi.org/10.1016/j.jmrt.2021.04.003.
[39] P. Badica, N.D. Batalu, M. Burdusel, M.A. Grigoroscuta, G. Aldica, M. Enculescu, G. Gradisteanu Pircalabioru, M. Popa, L.G. Marutescu, B.G. Dumitriu, L. Olariu, A. Bicu, B. Purcareanu, L. Operti, V. Bonino, A. Agostino, M. Truccato, M.C. Chifiriuc, Antibacterial composite coatings of MgB_2 powders embedded in PVP matrix, Sci. Rep. 11 (2021) 9591, http://dx.doi.org/10.1038/s41598-021-88885-2.
[40] P. Badica, N.D. Batalu, M.C. Chifiriuc, M. Burdusel, M.A. Grigoroscuta, G.V. Aldica, I. Pasuk, A. Kuncser, M. Popa, A. Agostino, L. Operti, S.K. Padhi, V. Bonino, M. Truccato, Sintered and 3D-printed bulks of MgB_2-based materials with antimicrobial properties, Molecules 26 (2021) 6045, http://dx.doi.org/10.3390/molecules26196045.
[41] S.K. Das, K. Jasuja, Chemical exfoliation of layered magnesium diboride to yield functionalized nanosheets and nanoaccordions for potential flame retardant applications, ACS Appl. Nano Mater. 1 (2018) 1612–1622, http://dx.doi.org/10.1021/acsanm.8b00101.
[42] T. Prozorov, R. Prozorov, A. Snezhko, K.S. Suslick, Sonochemical modification of the superconducting properties of MgB_2, Appl. Phys. Lett. 83 (2003) 2019–2021, http://dx.doi.org/10.1063/1.1609248.
[43] A. Yousaf, M.S. Gilliam, S.L.Y. Chang, M. Augustin, Y. Guo, F. Tahir, M. Wang, A. Schwindt, X.S. Chu, D.O. Li, S. Kale, A. Debnath, Y. Liu, M.D. Green, E.J.G. Santos, A.A. Green, Q.H. Wang, Exfoliation of quasi-two-dimensional nanosheets of metal diborides, J. Phys. Chem. C. 125 (2021) 6787–6799, http://dx.doi.org/10.1021/acs.jpcc.1c00394.
[44] S. Das, P. Sharma, Wavelength dependent photoionisation of ethanol clusters: Generation of hydrogen like C^{5+} ions at terawatt laser intensity, Phys. Chem. Chem. Phys. 24 (2022) 11979–11985, http://dx.doi.org/10.1039/D2CP00742H.
[45] M.-O. Mun, Y.J. Kim, Y. Park, J.H. Kim, S.H. Moon, H.N. Lee, H.G. Kim, B. Oh, Normal-state optical response functions of MgB2 superconductor, J. Supercond. 15 (2002) 475–477.
[46] Y. Fudamoto, S. Lee, Anisotropic electrodynamics of MgB_2 detected by optical reflectance, Phys. Rev. B. 68 (2003) 184514, http://dx.doi.org/10.1103/PhysRevB.68.184514.
[47] A.-G. Kussow, A. Akyurtlu, A. Semichaevsky, N. Angkawisittpan, MgB_2 -based negative refraction index metamaterial at visible frequencies: Theoretical analysis, Phys. Rev. B. 76 (2007) 195123, http://dx.doi.org/10.1103/PhysRevB.76.195123.
[48] A. Balassis, E.V. Chulkov, P.M. Echenique, V.M. Silkin, First-principles calculations of dielectric and optical properties of MgB_2, Phys. Rev. B. 78 (2008) 224502, http://dx.doi.org/10.1103/PhysRevB.78.224502.
[49] A.B. Kuzmenko, Multiband and impurity effects in infrared and optical spectra of MgB_2, Phys. C Supercond. 456 (2007) 63–74, http://dx.doi.org/10.1016/j.physc.2007.02.008.
[50] D. Di Castro, M. Ortolani, E. Cappelluti, U. Schade, N.D. Zhigadlo, J. Karpinski, Infrared properties of $Mg_{1-x}Al_x(B_{1-y}C_y)_2$ single crystals in the normal and superconducting state, Phys. Rev. B. 73 (2006) 174509, http://dx.doi.org/10.1103/PhysRevB.73.174509.
[51] T. Kakeshita, S. Lee, S. Tajima, Anisotropic drude response and the effect of anisotropic C substitution in $Mg(B_{1-x}c_x)_2$, Phys. Rev. Lett. 97 (2006) 037002, http://dx.doi.org/10.1103/PhysRevLett.97.037002.
[52] Y.-S. Seo, J.H. Lee, W.N. Kang, J. Hwang, Revisiting optical properties of MgB_2 with a high-quality sample prepared by a HPCVD method, Sci. Rep. 7 (2017) 8977, http://dx.doi.org/10.1038/s41598-017-09248-4.
[53] B. Balasubramanian, T. Maruyama, Evidence of an enhanced interband absorption in Au nanoparticles: Size-dependent electronic structure and optical properties, Appl. Phys. Lett. 87 (2005) http://dx.doi.org/10.1063/1.2077834.
[54] H.S. Zhou, I. Honma, H. Komiyama, J.W. Haus, Controlled synthesis and quantum-size effect in gold-coated nanoparticles, Phys. Rev. B. 50 (1994) 12052–12056, http://dx.doi.org/10.1103/PhysRevB.50.12052.
[55] E. Baldini, A. Mann, L. Benfatto, E. Cappelluti, A. Acocella, V.M. Silkin, S.V. Eremeev, A.B. Kuzmenko, S. Borroni, T. Tan, X.X. Xi, F. Zerbetto, R. Merlin, F. Carbone, Real-time observation of phonon-mediated $\sigma - \pi$ interband scattering in MgB_2, Phys. Rev. Lett. 119 (2017) 097002, http://dx.doi.org/10.1103/PhysRevLett.119.097002.
[56] J.A. Alarco, A. Chou, P.C. Talbot, I.D.R. Mackinnon, Phonon modes of MgB_2: Super-lattice structures and spectral response, Phys. Chem. Chem. Phys. 16 (2014) 24443–24456, http://dx.doi.org/10.1039/C4CP03449J.
[57] K.-P. Bohnen, R. Heid, B. Renker, Phonon dispersion and electron-phonon coupling in MgB_2 and AlB_2, Phys. Rev. Lett. 86 (2001) 5771–5774, http://dx.doi.org/10.1103/PhysRevLett.86.5771.
[58] A. Bateni, E. Erdem, W. Häßler, M. Somer, High-quality MgB_2 nanocrystals synthesized by using modified amorphous nano-boron powders: Study of defect structures and superconductivity properties, AIP Adv. 9 (2019) 045018, http://dx.doi.org/10.1063/1.5089488.
[59] L. Hai-Wen, K. Kikuchi, T. Sato, Y. Nakamori, N. Ohba, M. Aoki, K. Miwa, S. Towata, O. Shin-ichi, Synthesis and hydrogen storage properties of a single-phase magnesium borohydride $Mg(BH_4)_2$, Mater. Trans. 49 (2008) 2224–2228, http://dx.doi.org/10.2320/matertrans.MA200807.
[60] A. Bateni, Novel approach for synthesis of magnesium borohydride, $Mg(BH_4)_2$, Energy Procedia 29 (2012) 26–33, http://dx.doi.org/10.1016/j.egypro.2012.09.005.
[61] L. Ginés, S. Mandal, Ashek-I-Ahmed, C.-L. Cheng, M. Sow, O.A. Williams, Positive zeta potential of nanodiamonds, Nanoscale 9 (2017) 12549–12555, http://dx.doi.org/10.1039/C7NR03200E.